Radio Tomographic Imaging with Extremely Sparse and Location-Uncertain Transmitters

Angelo Coluccia
Department of Engineering
University of Salento
Lecce, Italy
angelo.coluccia@unisalento.it

Emanuele Mele
Department of Engineering
University of Salento
Lecce, Italy
emanuele.mele@unisalento.it

Alessio Fascista
Dept. of Electrical and Information Engineering
Politecnico di Bari
Bari, Italy
alessio.fascista@poliba.it

***Abstract*—Radio tomographic imaging (RTI) is an imaging technique that only uses received signal strength (RSS) measurements, classically on a dense mesh of transmitter-receiver (TX-RX) pairs with precisely known positions. However, in many practical scenarios, TX locations may be uncertain due to deployment constraints, mobility, or reliance on ambient RF sources. This paper investigates RTI in an extremely sparse setting, where only a few TXs (potentially just one) with uncertain positions are available, leading to a severe reduction in the number of TX-RX links and increased reconstruction challenges. We formulate the joint image reconstruction and TX localization problem and propose both optimal and suboptimal algorithms. The suboptimal algorithm, in particular, achieves near-optimal performance while maintaining linear complexity with respect to the number of TXs, in contrast to the exponential complexity of the optimal approach. Comparative evaluations against worst-case and stochastic robust approximation methods demonstrate the superior reconstruction accuracy of our proposed techniques.**

***Index Terms*—radio tomographic imaging, image reconstruction, received signal strength, localization.**

I. Introduction

Radiofrequency (RF) tomography is an imaging technique, particularly attractive when optical or acoustic methods are impractical [1]–[3]. Radio tomographic imaging (RTI) specifically leverages attenuation of RF signals — measured through received signal strength (RSS) — to infer the presence and location of objects within a monitored area [3], [4]. This means that no time or phase information about the signal is available; moreover, as opposed to much higher frequency waves (e.g., x-rays), significant non-line-of-sight (NLOS) propagation occurs. On the other hand, RSS measurements can be easily extracted from any low-cost off-the-shelf wireless device, making RTI an attractive solution for a variety of applications, e.g., people localization inside buildings, monitoring in smart home and smart city contexts, people counting and tracking [3]–[5], and passive localization [6].

In classical RTI, RSS measurements are collected between all transmitter-receiver (TX-RX) pairs, forming a full mesh of wireless nodes around the area of interest [3]–[7], as depicted in Fig. 1(a). Objects or people entering the scene induce variations in the RSS, enabling the reconstruction of spatial loss field (SLF) by solving an inverse problem. One of the fundamental assumptions in RTI (and tomography in general) is the precise knowledge of TX and RX positions [3]–[8].

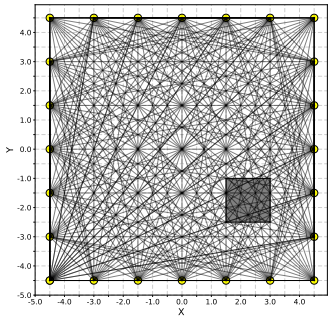

(a) Classical RTI: full-mesh TX-RX

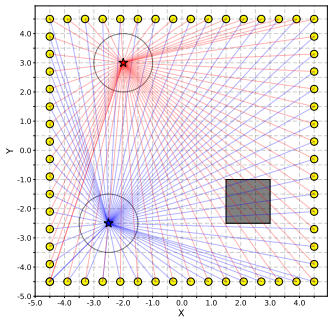

(b) Extremely sparse RTI: TXs (stars) with circular uncertainty region

Fig. 1: Classical vs. extremely sparse RTI. The square is a target of interest, small circles are measurement points (RXs).

However, in some scenarios, locations of TXs and/or RXs are uncertain due to factors such as deployment constraints, mobility, or the use of signals of opportunity. This uncertainty can severely degrade the quality of the reconstructed image. Recently, [9] started to address this issue by adopting stochastic robust approximation (SRA) [10, Sec. 6.4.1] and worst-case robust approximation (WCRA) [10, Sec. 6.4.2].

In this paper, we focus on an extremely sparse scenario where only a very small number of TXs (potentially as few as one) are available. This results in a significant reduction in the number of TX-RX pairs compared to full-mesh RTI, as shown in Fig. 1(b), leading to a substantial loss of information that makes imaging more challenging [11]. Furthermore, as discussed above, location uncertainty should be considered. While a similar setup has been explored in the context of pas-

sive RF tomography [12], [13], a critical distinction lies in the nature of the available data. In passive RF tomography, the full waveform can be exploited for image reconstruction via low-level signal processing. In contrast, RTI relies solely on power measurements (RSS), thus calling for a different approach. In this paper we formulate the RTI problem with extremely sparse and location-uncertain TXs, and propose both optimal and suboptimal algorithms, which are shown to significantly outperform the robust WCRA and SRA approaches.

II. RTI: Classical vs. Extremely Sparse Scenarios

For the sake of imaging, the area of interest is discretized into N voxels, i.e., pixels of the image to be reconstructed. Fig. 1 illustrates the resulting grid (dashed lines), where each voxel is associated with a physical position (conventionally, its center). The RTI problem typically assumes M measurement points surrounding the area of interest, which may correspond to M single RXs or to (one or) a few RXs moving around the perimeter (alike a synthetic aperture processing approach, *mutatis mutandis*). Irrespective of how RSS values are collected, in the conventional scenario each of the M measurement points also acts as a TX, forming a mesh with up to $L = M(M-1)$ distinct links, as illustrated in Fig. 1(a).

The RSS measurement associated with the i-th link (TX-RX pair), $i = 1, \dots, L$, follows the well-known path loss model for the average received power, possibly extended to account for wall attenuation in outdoor-to-indoor scenarios [14], and/or to incorporate frequency dependency when multi-channel links are considered [15]. In the RTI literature, variations between consecutive RSS acquisitions are mostly of concern, so as to get rid of static effects and reveal changes in the SLF [2]–[5], [7]–[9]. Any target present in the scene will occupy a certain number of voxels, depending on its size and shape, introducing an additional attenuation loss along the links that cross it. In Fig. 1, for instance, a square object located in the bottom-right part of the scene spans 9 voxels, leading to shadowing along the few links that intersect such voxels. The relationship between the link difference measurements $\boldsymbol{y} = [y_1 \cdots y_L]^\mathsf{T}$ (TX-RX pairs in arbitrary order) and the SLF values $\boldsymbol{x} = [x_1 \cdots x_N]^\mathsf{T}$ can be modeled as [2]–[5], [7]–[9]

$$\boldsymbol{y} = \boldsymbol{W}\boldsymbol{x} + \boldsymbol{n} \tag{1}$$

where the (i,j) entry of the weighting matrix $\boldsymbol{W} \in \mathbb{R}^{L \times N}$ captures the effect of the i-th link on the j-th voxel, while $\boldsymbol{n}$ stacks zero-mean noise terms with variance σ^2 (details on the noise distribution are given in Sec. IV). A popular computation for the values in $\boldsymbol{W}$ is via the elliptical model [2]–[5], [7]–[9], in which the weight of pixel j on link i is

$$W_{ij} = \begin{cases} \frac{1}{\sqrt{d_i}} & \text{if } d_{ij}^{\text{TX}} + d_{ij}^{\text{RX}} < d_i + \lambda \\ 0 & \text{otherwise} \end{cases} \tag{2}$$

where d_{ij}^{TX} and d_{ij}^{RX} are the distances from the j-th voxel to the TX-RX pair forming the i-th link, d_i is the distance between TX and RX for link i, and λ is the width of the ellipse (typically a small value, namely $\lambda = 0.007$ meters [3]).

Tomography is typically an ill-posed inverse problem, thus requiring regularization techniques. Under the Tikhonov approach, the image reconstruction problem is stated as

$$\hat{\boldsymbol{x}} = \arg\min_{\boldsymbol{x}} \|\boldsymbol{y} - \boldsymbol{W}\boldsymbol{x}\|^2 + \alpha\|\boldsymbol{Q}\boldsymbol{x}\|^2 \tag{3}$$

where $\|\cdot\|$ denotes the Euclidean norm hence $\|\boldsymbol{Q}\boldsymbol{x}\|^2 = \boldsymbol{x}^\mathsf{T}\boldsymbol{Q}^\mathsf{T}\boldsymbol{Q}\boldsymbol{x}$. Different choices of the regularization matrix $\boldsymbol{Q}$ are possible [2], [3] (further details are given in Sec. IV).

Finally, previous studies [4], [15] have shown that performance improves when employing multi-channel communications, i.e., by measuring RSS values across multiple channels for each link and combining them. Diversity in fact enhances reliability by ensuring that at least one channel remains in an anti-fade state, thereby enabling accurate attenuation measurements when the link LOS is obstructed.

Instead of the classical RTI setup, this paper considers an extremely-sparse scenario with very few TXs, i.e., $K \ll M$ (even as low as $K = 1$) in uncertain positions, as shown in Fig. 1(b). This means that the number of links is drastically reduced from $L = M(M-1)$, which scales quadratically with M, to only $L = KM$, which scales linearly with M (since K is a small constant), as apparent by comparing Fig. 1(a) and Fig. 1(b). Consequently, much less information is available to solve the image reconstruction problem. Furthermore, uncertainty in TX positions can degrade performance if not properly accounted for. In the next section, we formulate the joint RTI and TX position estimation problem, derive its optimal solution, and propose a low-complexity suboptimal algorithm.

III. Joint RTI and TX Position Estimation

We stack all the K unknown TX positions $\{\boldsymbol{p}_k\}_{k=1}^K \in \mathbb{R}^{2\times 1}$ in $\boldsymbol{p} = [\boldsymbol{p}_1^\mathsf{T} \cdots \boldsymbol{p}_K^\mathsf{T}]^\mathsf{T} \in \mathbb{R}^{2K\times 1}$, and assume that an uncertainty region $\boldsymbol{p}_k \in \mathcal{P}_k \subset \mathbb{R}^{2\times 1}$ is available, which represents a coarse prior information on each TX's position. Then, the joint estimation problem is

$$\hat{\boldsymbol{x}}^{\text{OPT}}, \hat{\boldsymbol{p}}^{\text{OPT}} = \arg\min_{\boldsymbol{x},\boldsymbol{p}} \|\boldsymbol{y} - \boldsymbol{W}(\boldsymbol{p})\boldsymbol{x}\|^2 + \alpha\|\boldsymbol{Q}\boldsymbol{x}\|^2 \tag{4}$$

where we have highlighted that now $\boldsymbol{W} \in \mathbb{R}^{KM\times N}$ depends upon $\boldsymbol{p}$ through d_i and d_{ij}^{TX}, via (2), and have omitted the variables' optimization domains to ease the notation. By minimizing over $\boldsymbol{x}$, treating it as a function of $\boldsymbol{p}$, we obtain

$$\hat{\boldsymbol{x}}^{\text{OPT}}(\boldsymbol{p}) = (\boldsymbol{W}^\mathsf{T}(\boldsymbol{p})\boldsymbol{W}(\boldsymbol{p}) + \alpha\boldsymbol{Q}^\mathsf{T}\boldsymbol{Q})^{-1}\boldsymbol{W}^\mathsf{T}(\boldsymbol{p})\boldsymbol{y} \tag{5}$$

which, plugged back in (4), returns

$$\begin{aligned} &\min_{\boldsymbol{p}} \min_{\boldsymbol{x}} \left\{ \|\boldsymbol{y} - \boldsymbol{W}(\boldsymbol{p})\boldsymbol{x}\|^2 + \alpha\|\boldsymbol{Q}\boldsymbol{x}\|^2 \right\} \\ &= \min_{\boldsymbol{p}} \left\| \left(\boldsymbol{I} - \boldsymbol{W}(\boldsymbol{p}) \left(\boldsymbol{W}^\mathsf{T}(\boldsymbol{p})\boldsymbol{W}(\boldsymbol{p}) + \alpha\boldsymbol{Q}^\mathsf{T}\boldsymbol{Q} \right)^{-1} \boldsymbol{W}^\mathsf{T}(\boldsymbol{p}) \right) \boldsymbol{y} \right\|^2 \end{aligned} \tag{6}$$

with $\boldsymbol{I}$ the identity matrix. Minimization over $\boldsymbol{p}$ does not admit a closed-form solution. Given the highly non-convex nature of the objective function (6), standard solvers are unable to find the global minimum, hence a $2K$-dimensional grid search is adopted to determine the optimal solution $\hat{\boldsymbol{p}}^{\text{OPT}}$ over $\mathcal{P}_k$s. The image is then reconstructed by plugging $\hat{\boldsymbol{p}}^{\text{OPT}}$ back in (5).

Unfortunately, the complexity of the search grows exponentially with the number of TXs K, making the optimal algorithm impractical even for small K, as it will be also discussed in the numerical results of Sec. IV.

To overcome this limitation, we consider a suboptimal approach that decouples the search over the K TX positions $\boldsymbol{p}_k \in \mathcal{P}_k$, by relaxing the problem formulation. Specifically, we decompose the problem into K independent subproblems, each focusing on a single TX. This involves processing a reduced version of (1), where instead of the full vector $\boldsymbol{y}$, only the M-dimensional subvector corresponding to the links involving the k-th TX is processed. By appropriately reordering and partitioning the variables as $\boldsymbol{y} = [\boldsymbol{y}_1^\mathsf{T} \cdots \boldsymbol{y}_K^\mathsf{T}]^\mathsf{T} \in \mathbb{R}^{KM\times 1}$, $\boldsymbol{W} = [\boldsymbol{W}_1^\mathsf{T} \cdots \boldsymbol{W}_K^\mathsf{T}]^\mathsf{T} \in \mathbb{R}^{KM\times N}$, and $\boldsymbol{n} = [\boldsymbol{n}_1^\mathsf{T} \cdots \boldsymbol{n}_K^\mathsf{T}]^\mathsf{T} \in \mathbb{R}^{KM\times 1}$, we obtain K submodels for $\boldsymbol{y}_k \in \mathbb{R}^{M\times 1}$ as follows

$$\boldsymbol{y}_k = \boldsymbol{W}_k \boldsymbol{x} + \boldsymbol{n}_k \tag{7}$$

hence in turn K suboptimal problems involving $\boldsymbol{W}_k \in \mathbb{R}^{M\times N}$

$$\hat{\boldsymbol{p}}_k^{\text{SUB}} = \arg\min_{\boldsymbol{p}_k} \left(\boldsymbol{W}_k^\mathsf{T}(\boldsymbol{p}_k)\boldsymbol{W}_k(\boldsymbol{p}_k) + \alpha \boldsymbol{Q}^\mathsf{T}\boldsymbol{Q} \right)^{-1} \boldsymbol{W}_k^\mathsf{T}(\boldsymbol{p}_k)\boldsymbol{y}_k \tag{8}$$

which can be all solved independently in $\boldsymbol{p}_k \in \mathcal{P}_k \subset \mathbb{R}^{2\times 1}$, for an overall complexity that scales linearly with K. Once the K TX position estimates $\hat{\boldsymbol{p}}_k^{\text{SUB}}$ are obtained, a single overall image reconstruction is finally performed by considering the original full-size problem, that is, by using (5) with $\boldsymbol{W}(\hat{\boldsymbol{p}}^{\text{SUB}})$ in place of $\boldsymbol{W}(\boldsymbol{p})$, where $\hat{\boldsymbol{p}}^{\text{SUB}} = [(\hat{\boldsymbol{p}}_1^{\text{SUB}})^\mathsf{T} \cdots (\hat{\boldsymbol{p}}_K^{\text{SUB}})^\mathsf{T}]^\mathsf{T} \in \mathbb{R}^{2K\times 1}$.

IV. Numerical Results

A. Simulation Setup

To evaluate the reconstruction performance, we consider a setup similar to that of Fig. 1(b), for both the single-TX case (using only the red TX) and the two-TX case (with both the red and blue TXs) as detailed below. The data $\boldsymbol{y}$ are generated based on the experimentally validated model in [3], with noise terms accounting for multipath fading variations; this means that the generation process is not matched to (1). Experiments in [3] indicate that RSS values vary slowly around a nearly constant mean but can also experience significant fading dips over certain periods. This behavior is well characterized by a two-state Markov chain, which alternates between low-variance and high-variance log-normal distributions.[1] Following [3], we adopt the same model parameters, generating noise terms (in dB) according to a two-component Gaussian mixture with standard deviations of 0.971 (weight 0.548) and 3.003 (weight 0.452). An attenuation of -20 dB is applied to links affected by shadowing due to the presence of a target.

As in most RTI literature, we adopt as regularizer $\boldsymbol{Q} = \boldsymbol{C}^{-1/2}$, where $\boldsymbol{C}$ is the covariance matrix of $\boldsymbol{x}$ whose (h,l) entry typically follows the exponential model [2]–[5], [7]–[9] $C_{hl} = \sigma_x^2 \mathrm{e}^{-d_{hl}/\delta_c}$ with d_{hl} the distance from pixel h to pixel l, δ_c is a "space constant" correlation parameter, and σ_x^2 is the pixel variance. We adopt the same parameters as in [3], i.e., $\delta_c = 1.3$ meters and $\sigma_x^2 = 0.1$ square dB. We set $\alpha = 1$.

We will compare the proposed algorithms against robust RTI approaches under position uncertainty [9], namely the SRA [10, Sec. 6.4.1] and WCRA [10, Sec. 6.4.2]. Such approaches need to be properly adapted to the extremely-sparse scenario considered here, as illustrated in the following.

B. Results for the Single-TX Case

We first consider the single-TX case, aiming at ascertaining to what extent imaging is still possible in such a challenging setup, where the available information is very scarce. We consider an area of 20×20 square meters with a spatial resolution of 0.5 meters, resulting in a discretized SLF $\boldsymbol{x}$ of size $N = 800$. The number of RX points is $M = 116$.

For a fair comparison, we assume a square uncertainty region of 2×2 square meters around the single TX for all algorithms, with a step size of 0.2 meters. This yields a grid of $P = 100$ 2-dimensional points, denoted as $\tilde{\boldsymbol{p}}^{(1)}, \ldots, \tilde{\boldsymbol{p}}^{(P)}$.

The WCRA approach minimizes the worst-case error within the uncertainty region, formulated as [10, Sec. 6.4.2]

$$\min_{\boldsymbol{x}} \max_{m=1,\ldots,P} \left\| \boldsymbol{y} - \boldsymbol{W}(\tilde{\boldsymbol{p}}^{(m)})\boldsymbol{x} \right\| \tag{9}$$

and then recast in equivalent epigraph form as

$$\min_{\boldsymbol{x},t} t \;\; \text{s.t.} \;\; \left\| \boldsymbol{y} - \boldsymbol{W}(\tilde{\boldsymbol{p}}^{(m)})\boldsymbol{x} \right\| \le t, \quad m = 1, \ldots, P. \tag{10}$$

This formulation results in a second-order cone programming problem, which is efficiently handled by standard solvers.

The SRA approach considers instead the minimization of the mean error [10, Sec. 6.4.1], i.e.,

$$\min_{\boldsymbol{x}} \mathrm{E} \left\| \boldsymbol{y} - \boldsymbol{W}(\tilde{\boldsymbol{p}}^{(m)})\boldsymbol{x} \right\| \tag{11}$$

which over the considered uncertainty region reads as

$$\min_{\boldsymbol{x}} \sum_{m=1}^{P} \pi_m \left\| \boldsymbol{y} - \boldsymbol{W}(\tilde{\boldsymbol{p}}^{(m)})\boldsymbol{x} \right\| \tag{12}$$

where π_m is the probability associated with point $\tilde{\boldsymbol{p}}^{(m)}$, with the constraint $\sum_{m=1}^{P} \pi_m = 1$. Assuming a uniform distribution over the uncertainty region ($\pi_m = 1/P$), (12) can be rewritten in epigraph form as a sum-of-norms problem:

$$\min_{\boldsymbol{x},\boldsymbol{t}} \mathbf{1}^\mathsf{T}\boldsymbol{t} \;\; \text{s.t.} \left\| \boldsymbol{y} - \boldsymbol{W}(\tilde{\boldsymbol{p}}^{(m)})\boldsymbol{x} \right\| \le t_m, \;\; m = 1, \ldots, P \tag{13}$$

where $\boldsymbol{t} = [t_1 \cdots t_P]^\mathsf{T}$ and $\mathbf{1}$ denoting the vector of ones. Like the WCRA, this is a second-order cone programming problem that can be solved using standard numerical methods.

Fig. 2 presents the reconstructed images from left to right: the "oracle" (which uses the exact TX position), the proposed approach, and the two competitors WCRA and SRA — in the single-TX case, suboptimal algorithms obviously boil down to the corresponding optimal ones. Notably, even the oracle reconstruction reveals the inherent difficulty of the single-TX case, as evidenced by the presence of a "streak" pattern in Fig. 2(a), which suggests ambiguities in mapping the presence of the target. Still, the proposed approach provides a satisfactory

[1] As observed in [3], both the log-normal distribution and the logarithm of a Rician distribution (since RSS values are expressed in dB) provide a good fit for experimental data due to their similar shapes.

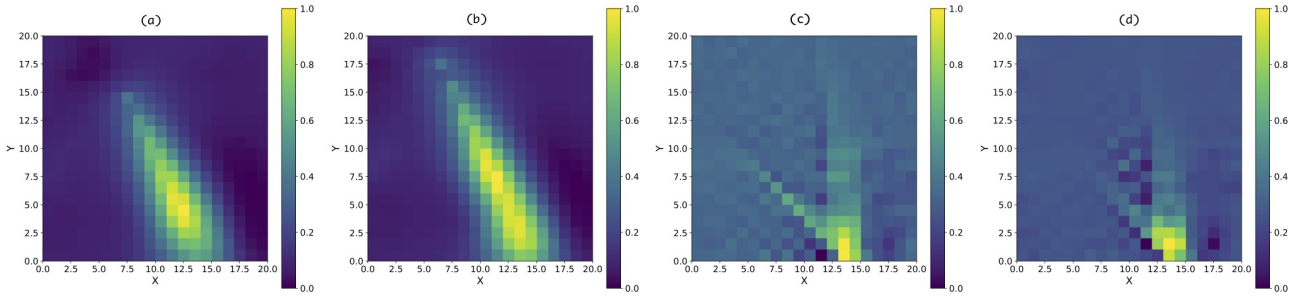

Fig. 2: Reconstructed images for the single-TX case: (a) "oracle" reconstruction using the exact TX position; (b) proposed approach; (c) WCRA and (d) SRA.

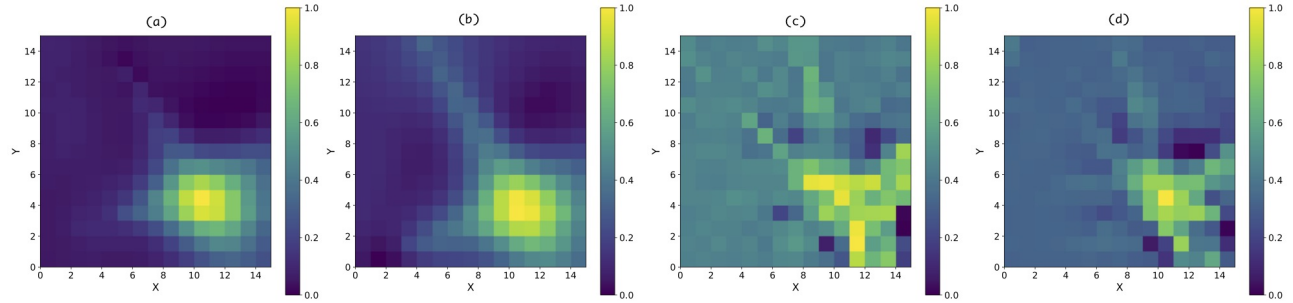

Fig. 3: Reconstructed images for the two-TX case: (a) "oracle" reconstruction using the two exact TXs positions; optimal versions of the (b) proposed approach, (c) WCRA, and (d) SRA.

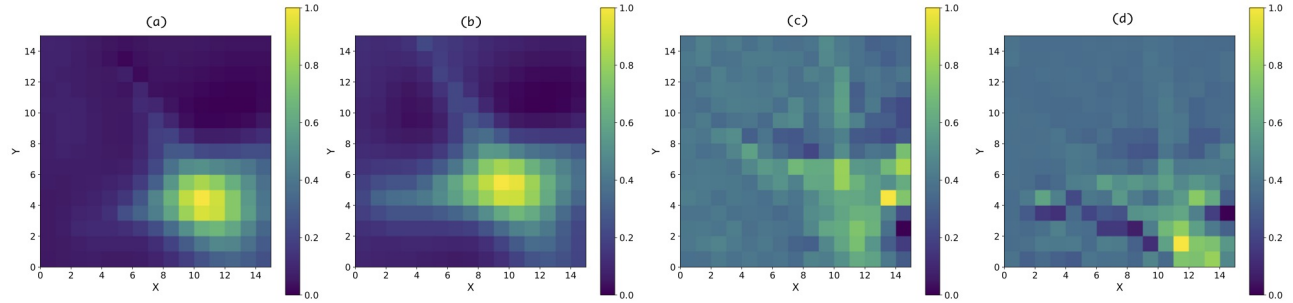

Fig. 4: Reconstructed images for the two-TX case: (a) "oracle" reconstruction using the two exact TXs positions; suboptimal versions of the (b) proposed approach, (c) WCRA, and (d) SRA.

image reconstruction, qualitatively close to that of the oracle. In contrast, the competitors yield more "noisy" images.

C. Results for the Two-TX Case

We now consider the case of two TXs ($K = 2$). Again, for a fair comparison, all algorithms assume a square uncertainty region of 2×2 square meters around each TX, with step 0.2 meters, resulting in a joint search grid of $P = 100$ $2K$-dimensional points $\tilde{\boldsymbol{p}}^{(m)}$. In other words, the search is conducted over P possible pairs of TXs, each represented as a $2K$-tuple of coordinates, i.e., $\tilde{\boldsymbol{p}}^{(m)} = [\tilde{\boldsymbol{p}}_1^{(m)\mathsf{T}} \cdots \tilde{\boldsymbol{p}}_K^{(m)\mathsf{T}}]^{\mathsf{T}}$, $m = 1, \ldots, P$. For $K = 2$, the resulting 4-dimensional search space is computationally intensive, making it impractical to compute the optimal versions of the algorithms (both proposed and competitors). Indeed, as discussed earlier, suboptimal algorithms are needed. However, to evaluate the possible loss in reconstruction accuracy, we consider a reduced-size scenario where computation of optimal algorithms is still viable; specifically, an area of 15×15 square meters corresponding to $N = 112$, and $M = 120$ RX points.

For a thorough assessment, we add to the analysis suboptimal versions of SRA and WCRA. As to the latter, for a fair comparison we consider the same matrix partitioning as in Sec. III, which leads to an optimization problem similar to (10) but with KP constraints (instead of P) and reduced-size subvectors and submatrices as in (7), i.e.

$$\min_{\boldsymbol{x},t} t \;\; \text{s.t.} \;\; \left\| \boldsymbol{y}_k - \boldsymbol{W}_k(\tilde{\boldsymbol{p}}^{(m)})\boldsymbol{x} \right\| \leq t, \qquad \begin{matrix} m = 1, \ldots, P \\ k = 1, \ldots, K \end{matrix} .$$

As to SRA in (13), its suboptimal version is likewise obtained:

$$\min_{\boldsymbol{x},\boldsymbol{t}} \mathbf{1}^{\mathsf{T}}\boldsymbol{t} \;\; \text{s.t.} \;\; \left\| \boldsymbol{y}_k - \boldsymbol{W}_k(\tilde{\boldsymbol{p}}^{(m)})\boldsymbol{x} \right\| \leq t_m, \qquad \begin{matrix} m = 1, \ldots, P \\ k = 1, \ldots, K \end{matrix} .$$

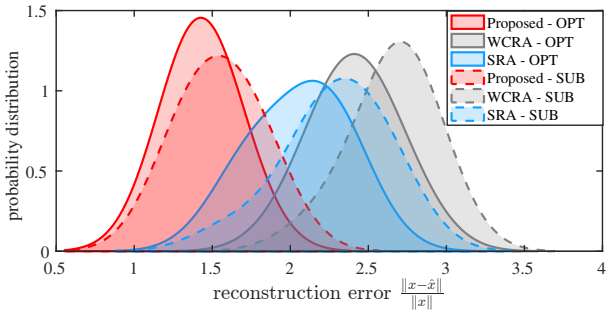

Fig. 5: Distributions of the reconstruction errors.

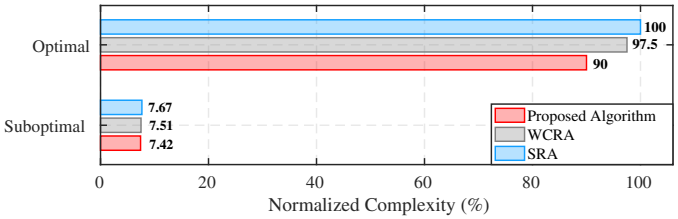

Fig. 6: Average elapsed-time computational complexity.

Fig. 3 reports the reconstructed images for the two-TX case, comparing the optimal versions of the proposed approach, WCRA, and SRA, with the "oracle" (exact TXs positions). The reconstruction accuracy achieved by the oracle in Fig. 3(a) is notably superior to its single-TX counterpart in Fig. 2(a). This confirms that incorporating just one additional TX considerably improves the reconstruction quality. Remarkably, Fig. 3(b) shows that the optimal proposed algorithm achieves a reconstruction accuracy very close to that of the oracle, despite the additional challenge of estimating the two unknown TX positions, and outperforms both the WCRA and SRA.

Fig. 4 shows instead the results for the suboptimal algorithms, again in comparison with the oracle. Remarkably, the proposed suboptimal approach achieves near-optimal performance, whereas the two competing methods exhibit significantly poorer reconstruction quality.

Finally, ten different target positions are considered to quantitatively assess both reconstruction accuracy and complexity. Fig. 5 illustrates the estimated probability distributions of the reconstruction errors, computed as $\frac{\|\boldsymbol{x}-\hat{\boldsymbol{x}}\|}{\|\boldsymbol{x}\|}$, using the kernel density method. The results clearly demonstrate that the proposed approach consistently outperforms the competitors, achieving near-optimal performance. Moreover, this is accomplished with a significantly lower computational burden: indeed, as also discussed in Sec. III, optimal resolution of the RTI problem under TX position uncertainty comes with increased computational complexity due to the expansion of the search space — in this case from two to four dimensions. To show further evidence of the computational advantage of the suboptimal approach, Fig. 6 presents the relative reduction in average computational time, with 100% representing the most time-consuming algorithm (SRA). Once again, the suboptimal approach achieves a remarkable computational saving compared to the optimal solution(s), while still delivering near-optimal performance.

V. Conclusion

We have addressed the RTI problem in the challenging scenario of extremely sparse and location uncertain TXs, deriving both optimal and suboptimal algorithms for joint image reconstruction and TX position estimation. Results show that RTI remains feasible even with a single TX. Moreover, the proposed algorithms significantly outperforms state-of-the-art robust approaches, with the suboptimal version achieving near-optimal performance at a fraction of the computational complexity, scaling linearly with the number of TXs as opposed to the exponential complexity of the optimal approach.

References

[1] C. R. Anderson, R. K. Martin, T. O. Walker, and R. W. Thomas, "Radio Tomography for Roadside Surveillance," *IEEE Journal of Selected Topics in Signal Processing*, vol. 8, no. 1, pp. 66–79, 2014.

[2] D. Lee, D. Berberidis, and G. B. Giannakis, "Adaptive Bayesian Radio Tomography," *IEEE Transactions on Signal Processing*, vol. 67, no. 8, pp. 1964–1977, 2019.

[3] J. Wilson and N. Patwari, "Radio Tomographic Imaging with Wireless Networks," *IEEE Transactions on Mobile Computing*, vol. 9, no. 5, pp. 621–632, 2010.

[4] C. Alippi, M. Bocca, G. Boracchi, N. Patwari, and M. Roveri, "RTI Goes Wild: Radio Tomographic Imaging for Outdoor People Detection and Localization," *IEEE Transactions on Mobile Computing*, vol. 15, no. 10, pp. 2585–2598, 2016.

[5] Y. Lu, Y. Ma, W. Ning, and H. Zhao, "Multitarget Localization for RTI Based on Constructing Feature Region Combination," *IEEE Sensors Journal*, vol. 23, no. 17, pp. 20 002–20 011, 2023.

[6] M. Jabbar and U. Shoaib, "Passive localization based on radio tomography images with CNN model utilizing WIFI RSSI," *Scientific Reports*, vol. 15, no. 1, pp. 1–16, 2025.

[7] M. Bocca, O. Kaltiokallio, and N. Patwari, "Radio tomographic imaging for ambient assisted living," in *Evaluating AAL Systems Through Competitive Benchmarking: International Competitions and Final Workshop, EvAAL 2012, July and September 2012. Revised Selected Papers 2*. Springer, 2013, pp. 108–130.

[8] D. Romero, D. Lee, and G. B. Giannakis, "Blind Radio Tomography," *IEEE Transactions on Signal Processing*, vol. 66, no. 8, pp. 2055–2069, 2018.

[9] A. Mishra, U. K. Sahoo, and S. Maiti, "Robust radio tomographic imaging for localization of targets under uncertain sensor location scenario," *Digital Signal Processing*, vol. 137, p. 104030, 2023.

[10] S. Boyd and L. Vandenberghe, *Convex Optimization*. Cambridge University Press, 2004.

[11] Z. Li, A. Dubey, S. Shen, N. K. Kundu, J. Rao, and R. Murch, "Radio Tomographic Imaging With Reconfigurable Intelligent Surfaces," *IEEE Transactions on Wireless Communications*, vol. 23, no. 11, pp. 15 784–15 797, 2024.

[12] L. Lo Monte, D. Erricolo, F. Soldovieri, and M. C. Wicks, "Radio Frequency Tomography for Tunnel Detection," *IEEE Transactions on Geoscience and Remote Sensing*, vol. 48, no. 3, pp. 1128–1137, 2010.

[13] T. M. Tran, A. J. Terzuoli, G. J. Scalzi, and L. Lo Monte, "Toward passive RF tomography: Signal processing and experimental validation," in *2014 IEEE Radar Conference*, 2014, pp. 869–874.

[14] I. Rodriguez, H. C. Nguyen, I. Z. Kovács, T. B. Sørensen, and P. Mogensen, "An empirical outdoor-to-indoor path loss model from below 6 ghz to cm-wave frequency bands," *IEEE Antennas and Wireless Propagation Letters*, vol. 16, pp. 1329–1332, 2017.

[15] O. Kaltiokallio, M. Bocca, and N. Patwari, "Enhancing the accuracy of radio tomographic imaging using channel diversity," in *2012 IEEE 9th International Conference on Mobile Ad-Hoc and Sensor Systems (MASS 2012)*, 2012, pp. 254–262.